

Generative modeling of conditional probability distributions on the level-sets of collective variables

Fatima-Zahrae Akhyar* Wei Zhang† Gabriel Stoltz‡ Christof Schütte§

Abstract

Given a probability distribution μ in \mathbb{R}^d represented by data, we study in this paper the generative modeling of its conditional probability distributions on the level-sets of a collective variable $\xi : \mathbb{R}^d \rightarrow \mathbb{R}^k$, where $1 \leq k < d$. We propose a general and efficient learning approach that is able to learn generative models on different level-sets of ξ simultaneously. To improve the learning quality on level-sets in low-probability regions, we also propose a strategy for data enrichment by utilizing data from enhanced sampling techniques. We demonstrate the effectiveness of our proposed learning approach through concrete numerical examples. The proposed approach is potentially useful for the generative modeling of molecular systems in biophysics, for instance.

Keywords— collective variables, level-sets, conditional probability distributions, generative modeling, flow-matching

1 Introduction

High-dimensional stochastic processes are ubiquitous in broad research areas such as biophysics, materials science, and climate modeling. Understanding the complex dynamical behavior of such processes often requires projecting the system down to a (much) lower-dimensional space via a few features, i.e. collective variables (CVs) or reaction coordinates, of the system. In molecular dynamics, for instance, various enhanced sampling techniques have been developed to overcome the sampling difficulty due to the system’s metastability and to construct the free energy surface in the space of CVs [15]. A number of analytical and computational approaches have also been proposed for constructing simpler, lower-dimensional surrogate models associated to a chosen set of CVs of the original high-dimensional system. One notable approach is the effective dynamics constructed using conditional expectations, where the coefficients (i.e. drift and diffusion) in the surrogate model are computed by taking averages with respect to the so-called conditional probability distribution on the corresponding level-set of the CVs [21]. This approach has attracted considerable research interest in the mathematical community [50, 51, 22, 29, 23, 9, 52], contributing to a deeper understanding of the quality of the effective dynamics in approximating the original high-dimensional processes.

A related research topic in molecular dynamics is sampling on the level-sets of CVs [5, 13, 26], which is useful in both of the aforementioned tasks, i.e. free energy computation and computing the coefficients in the effective dynamics. Metropolis-Hastings Monte Carlo methods have been developed for unbiased sampling on submanifolds defined by the level-sets of CVs [48, 27, 28]. Given a (Boltzmann–Gibbs) distribution in the full space, sampling methods for its conditional distribution on the level-sets of CVs have been developed by constructing ergodic diffusion processes on the level-sets [49, 42]. More broadly, methods for sampling under constraints have also been studied in computational statistics [46, 35].

In recent years, generative modeling approaches, in particular diffusion models [43, 17, 44, 45] and flow-matching models [31, 32, 1], have achieved significant success in a wide range of real-world applications. Motivated by these achievements, there has been growing research interest in extending generative modeling approaches for Euclidean data to manifold data [36, 41, 2, 8, 18, 19, 4, 34, 33]. However, to the best of our knowledge, most of these existing approaches rely on substantial geometric information such as geodesics [8], heat kernel, or eigenfunctions [4], which

*Zuse Institute Berlin, Takustrasse 7, Berlin 14195, Germany; Email: fatima-zahrae.akhyar@enpc.fr

†Zuse Institute Berlin, Takustrasse 7, Berlin 14195, Germany; Email: zhang@zib.de

‡CERMICS, ENPC, Institut Polytechnique de Paris, Marne-la-Vallée, France; MATERIALS team-project, Inria Paris, France; Email: gabriel.stoltz@enpc.fr

§Institute of Mathematics, Freie Universität Berlin, Arnimalle 6, Berlin 14195, Germany; Zuse Institute Berlin, Takustrasse 7, Berlin 14195, Germany; Email: schuette@zib.de

consequently limits their applicability to manifolds where such information is explicitly known. Only the methods proposed in [34, 33] can be applied to manifolds that are implicitly defined as a level-set of a certain function. All these approaches are developed for generative modeling on a single and fixed manifold.

In this paper, we study the generative modeling of conditional probability distributions on the level-sets of CVs and propose a versatile framework for this task. Our approach builds upon the flow-matching model [31, 32, 1], in which a neural ordinary differential equation (ODE) is learned to transport samples from a base Gaussian distribution to the target conditional distribution on each level-set of a CV map ξ . Our method does not require explicit geometric information of the underlying manifolds and therefore is broadly applicable to a wide range of manifolds implicitly defined by CVs. Moreover, by varying the target CV value, the method can generate samples across different level-sets of ξ , rather than being restricted to a single level-set. To further improve learning in regions of low probability density, we introduce a data enrichment strategy that leverages data obtained from enhanced sampling techniques such as adaptive biasing force (ABF) simulations. The approach is validated on a hierarchy of systems of increasing complexity, from synthetic low-dimensional examples to high-dimensional molecular datasets. The main contributions of this paper are summarized below:

- (i) a **general and efficient generative modeling framework** capable of learning conditional distributions on families of manifolds implicitly defined by CVs;
- (ii) a **data enrichment strategy** that utilizes enhanced sampling data to improve accuracy in low-density regions; and
- (iii) **comprehensive numerical validations** that demonstrate the flexibility, robustness, and practical applicability of the method to molecular systems.

The remainder of the paper is organized as follows. In Section 2, we present the theoretical background and introduce the relevant notation. Section 3 details the proposed generative modeling methodology. In Section 4, we apply our approach to a series of representative datasets to illustrate its performance and generality. Finally, Section 5 concludes the paper and outlines possible directions for future research.

2 Background and notation

The aim of this section is to introduce the probability distributions of interest in this work, in particular the conditional distribution on the level-sets of a given smooth map, which will play a central role in the following.

Consider a target distribution μ over \mathbb{R}^d with a positive probability density ρ with respect to the Lebesgue measure, namely $\mu(dx) = \rho(x) dx$. Assume that a C^2 -smooth map $\xi : \mathbb{R}^d \rightarrow \mathbb{R}^k$ is given, where $1 \leq k < d$. We are particularly interested in applications in statistical physics, where μ arises as the invariant distribution of certain ergodic diffusion processes x_t in \mathbb{R}^d and ξ corresponds to the CV of the system. In this case, we often refer to the Boltzmann–Gibbs distribution, whose density with respect to the Lebesgue measure is

$$\rho(x) = \frac{1}{Z} e^{-\beta V(x)}, \quad x \in \mathbb{R}^d, \quad (1)$$

where $V : \mathbb{R}^d \rightarrow \mathbb{R}$ is a smooth potential function that grows sufficiently fast to infinity as $|x| \rightarrow +\infty$, β is a positive constant whose inverse is proportional to the system’s temperature, and $Z = \int_{\mathbb{R}^d} e^{-\beta V(x)} dx$ is the normalizing constant. We introduce a few quantities related to the measure μ and the map ξ . Further discussions can be found in [25, Section 3.2.1] and [50].

Given $z \in \mathbb{R}^k$, we define $\Sigma_z := \{x \in \mathbb{R}^d \mid \xi(x) = z\}$ as the level-set of the map ξ . Assume that Σ_z is non-empty and that the Jacobian of ξ at x , denoted by $\nabla \xi(x) \in \mathbb{R}^{d \times k}$, has full rank k at each $x \in \Sigma_z$. Under this assumption, the regular value theorem implies that Σ_z is a $(d - k)$ -dimensional submanifold of \mathbb{R}^d ; see [16, Chapter 1, Theorem 3.2]. Let $\tilde{\mu}$ denote the pushforward measure of μ by the map ξ ; that is, $\tilde{\mu}$ is the probability measure of the random variable $\xi(X) \in \mathbb{R}^k$ when $X \sim \mu$. Let μ_z denote the conditional probability measure on Σ_z . The law of total expectation implies

$$\mathbb{E}_\mu(f(X)) = \mathbb{E}_{z \sim \tilde{\mu}} \left[\mathbb{E}_{X \sim \mu} (f(X) \mid \xi(X) = z) \right] = \mathbb{E}_{z \sim \tilde{\mu}} \left[\mathbb{E}_{X \sim \mu_z} (f(X)) \right], \quad (2)$$

for a test function $f : \mathbb{R}^d \rightarrow \mathbb{R}$. Moreover, the co-area formula implies that (see [10, Theorem 3.11] and [25, Lemma 3.2])

$$\mu_z(dx) = \frac{1}{Q(z)} \rho(x) \det(\nabla \xi(x)^\top \nabla \xi(x))^{-\frac{1}{2}} \sigma_{\Sigma_z}(dx), \quad x \in \Sigma_z, \quad (3)$$

and

$$\tilde{\mu}(dz) = Q(z) dz, \quad z \in \mathbb{R}^k, \quad (4)$$

where σ_{Σ_z} denotes the surface measure of Σ_z and

$$Q(z) = \int_{\Sigma_z} \rho(x) \det(\nabla \xi(x)^\top \nabla \xi(x))^{-\frac{1}{2}} \sigma_{\Sigma_z}(dx), \quad z \in \mathbb{R}^k, \quad (5)$$

is a normalizing factor in (3). For processes whose invariant distribution is the Boltzmann–Gibbs distribution $\mu(dx) = \frac{1}{Z} e^{-\beta V(x)} dx$, the free energy associated with the map ξ is defined as

$$F(z) = -\beta^{-1} \ln Q(z), \quad z \in \mathbb{R}^k, \quad (6)$$

and, from (4), we have

$$\tilde{\mu}(dz) = e^{-\beta F(z)} dz, \quad z \in \mathbb{R}^k. \quad (7)$$

3 Learning approach

In this section, we present our methodology for learning generative models on the level-sets of a smooth map ξ . We first describe the standard approach based on flow-matching for learning the conditional distributions μ_z corresponding to different values $z \in \mathbb{R}^k$. Then, we discuss an enhanced learning strategy that leverages biased trajectory data to improve the quality of the learning in regions of low probability under the pushforward distribution $\tilde{\mu}$. Finally, we explain how such biased trajectory data can be generated in practice using adaptive biasing techniques.

3.1 Standard learning approach

Our goal is to sample the conditional probability measure μ_z on the level-sets of ξ for different values $z \in \mathbb{R}^k$. For this purpose, we adopt the flow-matching generative modeling framework [32, 31, 1], which employs ordinary differential equations (ODEs) in \mathbb{R}^d

$$\frac{dX_t}{dt} = v(X_t, t), \quad X_0 \sim \nu_{\text{prior}}, \quad t \in [0, 1] \quad (8)$$

to transform a prior distribution ν_{prior} to a target distribution ν that is represented by data. For this purpose, the vector field v in (8) is learned by minimizing the standard flow-matching objective [32]

$$\mathcal{L}_{\text{FM}, \nu}(v) = \mathbb{E}_{t \sim U([0,1])} \mathbb{E}_{X_0 \sim \nu_{\text{prior}}, X_1 \sim \nu} \|v((1-t)X_0 + tX_1, t) - (X_1 - X_0)\|^2. \quad (9)$$

It is known that the minimizer of (9) leads to an ODE (8) that transforms the prior distribution ν_{prior} to the target ν .

Adapting this framework to our setting, we propose to learn the ODEs

$$\frac{dX_t}{dt} = v^{(z)}(X_t, t), \quad X_0 \sim \nu_{\text{prior}}, \quad t \in [0, 1], \quad (10)$$

parametrized by a variable $z \in \mathbb{R}^k$, such that, for a fixed $z \in \mathbb{R}^k$, the system (10) transforms the prior distribution from $t = 0$ to the conditional measure μ_z at $t = 1$. To achieve this goal, we consider the following objective for learning the vector field in (10):

$$\mathcal{L}(v) = \mathbb{E}_{t \sim U([0,1])} \mathbb{E}_{X_0 \sim \nu_{\text{prior}}, X_1 \sim \mu} \left\| v^{(\xi(X_1))}((1-t)X_0 + tX_1, t) - (X_1 - X_0) \right\|^2, \quad (11)$$

where μ is the probability distribution introduced in the previous section. To justify (11), notice that we can derive

$$\begin{aligned} \mathcal{L}(v) &= \mathbb{E}_{X_1 \sim \mu} \mathbb{E}_{t \sim U([0,1]), X_0 \sim \nu_{\text{prior}}} \left\| v^{(\xi(X_1))}((1-t)X_0 + tX_1, t) - (X_1 - X_0) \right\|^2 \\ &= \mathbb{E}_{z \sim \tilde{\mu}} \left[\mathbb{E}_{t \sim U([0,1])} \mathbb{E}_{X_0 \sim \nu_{\text{prior}}, X_1 \sim \mu_z} \left\| v^{(z)}((1-t)X_0 + tX_1, t) - (X_1 - X_0) \right\|^2 \right] \\ &= \mathbb{E}_{z \sim \tilde{\mu}} \left(\mathcal{L}_{\text{FM}, \mu_z}(v^{(z)}) \right), \end{aligned} \quad (12)$$

where the second equality follows from the law of total expectation in (2). This implies that minimizing the objective (11) is equivalent to minimizing the standard flow-matching objective (9) simultaneously for different target distributions μ_z . Therefore, it allows us to learn the ODE (10) for generative modeling on level-sets Σ_z corresponding to different values z at the same time.

In practice, (11) is replaced by the empirical objective

$$\mathcal{L}^{(N)}(v) = \frac{1}{N} \sum_{n=1}^N \left\| v^{(\xi(X^{(n)}))}((1-t_n)X_0^{(n)} + t_n X^{(n)}, t) - (X^{(n)} - X_0^{(n)}) \right\|^2, \quad (13)$$

where t_1, t_2, \dots, t_N are drawn independently from $U([0, 1])$, $X_0^{(1)}, X_0^{(2)}, \dots, X_0^{(N)}$ are drawn independently from ν_{prior} , and $X^{(1)}, X^{(2)}, \dots, X^{(N)}$ are the data points.

3.2 Enhanced learning approach with biased trajectory data

We consider the case where the target distribution μ is the Boltzmann–Gibbs distribution in (1), which is the invariant distribution of a diffusion process x_t in \mathbb{R}^d . For simplicity, we assume that x_t is governed by the overdamped Langevin dynamics

$$dx_t = -\nabla V(x_t) dt + \sqrt{2\beta^{-1}} dw_t, \quad t \geq 0, \quad (14)$$

where $V : \mathbb{R}^d \rightarrow \mathbb{R}$ is a smooth potential function that increases to infinity sufficiently fast as $|x| \rightarrow +\infty$ and w_t is a standard Brownian motion in \mathbb{R}^d . In this case, it is known that the Boltzmann–Gibbs distribution μ in (1) is invariant under the process x_t in (14) and that x_t is ergodic with respect to μ . Thanks to the ergodicity of the process, the empirical objective can be evaluated from trajectory data $X^{(1)}, X^{(2)}, \dots, X^{(N)}$ obtained by sampling (14) using a numerical scheme at time $t = h, 2h, \dots, Nh$, where h denotes the step-size and N is the total number of sampling steps.

We are particularly interested in the case where the potential V has multiple local minima and β is (relatively) large. In this case, the probability density of the invariant distribution μ is highly non-uniform in space, since the probability that x_t is within the vicinity of one of the local minima (metastable regions) is much larger than the probability that x_t is elsewhere. Likewise, for a proper CV map ξ , the pushforward distribution $\tilde{\mu}$ of μ defined in (4) is highly non-uniform in \mathbb{R}^k as well. In this case, the generative model that is learned by minimizing the objective (11) (or its empirical counterpart (13)) using training data sampled from (14) may be inferior for values z that belong to low-density regions under $\tilde{\mu}$, due to the relatively small contribution of the loss in such regions to the aggregated objective (11) (see (12)).

In order to overcome the aforementioned issue, we utilize the observation (as can be seen from the derivation (12)) that different probability distributions of X_1 can be chosen in (11), as long as the corresponding conditional probability distributions coincide with the conditional probability distributions μ_z of μ . In particular, let us consider the reweighted (RW) probability distribution defined by

$$\mu_{\text{RW}}(dx) = \bar{Z}^{-1} Z^{-1} e^{-\beta(V(x) - A(\xi(x)))} dx, \quad x \in \mathbb{R}^d, \quad (15)$$

where $A : \mathbb{R}^k \rightarrow \mathbb{R}$ and $\bar{Z} = Z^{-1} \int_{\mathbb{R}^d} e^{-\beta(V(x) - A(\xi(x)))} dx$ is a normalizing factor. Then, for each $z \in \mathbb{R}^k$, it is straightforward to verify that the conditional probability distribution of μ_{RW} on the level-set Σ_z is μ_z given in (3). Moreover, using (5) and (6), we can obtain that the pushforward of μ_{RW} by the map ξ satisfies

$$\tilde{\mu}_{\text{RW}}(dz) = \bar{Z}^{-1} e^{-\beta(F(z) - A(z))} dz, \quad z \in \mathbb{R}^k, \quad (16)$$

where F is the free energy (6) associated to the map ξ . With the choice of the probability distribution μ_{RW} in (15), the objective (11) becomes

$$\mathcal{L}_{\text{RW}}(v) = \mathbb{E}_{t \sim U([0,1])} \mathbb{E}_{X_0 \sim \nu_{\text{prior}}, X_1 \sim \mu_{\text{RW}}} \left\| v^{(\xi(X_1))} ((1-t)X_0 + tX_1, t) - (X_1 - X_0) \right\|^2, \quad (17)$$

and by analogy with (18) we can derive that

$$\mathcal{L}_{\text{RW}}(v) = \mathbb{E}_{z \sim \tilde{\mu}_{\text{RW}}} (\mathcal{L}_{\text{FM}, \mu_z}(v^{(z)})). \quad (18)$$

From (16), we can see that the density of $\tilde{\mu}_{\text{RW}}$ is more uniform than the density of $\tilde{\mu}$ in (7) when A is close to the free energy F . Therefore, (18) implies that in this case the contribution of the loss for values z in low-density regions under $\tilde{\mu}$ is enhanced in the objective (17).

To generate training data, we notice that μ_{RW} in (15) is the invariant distribution of the process

$$dx_t = -\nabla(V - A \circ \xi)(x_t) dt + \sqrt{2\beta^{-1}} dw_t, \quad t \geq 0. \quad (19)$$

To ensure that A approximates the free energy F , we adopt the adaptive biasing force (ABF) method [7, 14, 11, 6, 30]. Concretely, we generate training data by simulating the biased process

$$dx_t = -\nabla V(x_t) dt + \nabla \xi(x_t) f_t(\xi(x_t)) dt + \sqrt{2\beta^{-1}} dw_t, \quad t \geq 0, \quad (20)$$

where $f_t(z)$ is an estimation of the gradient of the free energy F (i.e. the mean force), based on the expression [25, Lemma 3.9]:

$$\frac{\partial F}{\partial z_i}(z) = \mathbb{E}_{\mu_z} \left[\sum_{l=1}^d \sum_{j=1}^k (\nabla \xi^\top \nabla \xi)^{-1}_{lj} \frac{\partial \xi_j}{\partial x_l} \frac{\partial V}{\partial x_l} - \beta^{-1} \sum_{l=1}^d \frac{\partial}{\partial x_l} \left(\sum_{j=1}^k (\nabla \xi^\top \nabla \xi)^{-1}_{lj} \frac{\partial \xi_j}{\partial x_l} \right) \right], \quad i = 1, 2, \dots, k, \quad (21)$$

where $(\nabla\xi^\top\nabla\xi)_{ij}^{-1}$ denotes the ij -component of the inverse of the matrix $\nabla\xi^\top\nabla\xi \in \mathbb{R}^{k \times k}$. In practice, a grid in \mathbb{R}^k is defined and the mean value (21) is estimated for each cell of the grid. In each simulation step, the estimation is updated for the cell which the current state $\xi(x_t)$ falls into. When the cell has been visited for more than a certain (pre-defined) number of times, the current value of the estimation is used as the biasing term $f_t(\xi(x_t))$ in (20). As $t \rightarrow +\infty$, we can expect that the empirical estimations converge to the true means in (21) and, accordingly, the process (20) converges to its equilibrium counterpart (19) with $A = F$.

3.3 Projection step

Once the model is learned using the approach described in the previous subsection, it can be used to generate new data points on different target level-sets of ξ by integrating the ODE (10) with different values $z \in \mathbb{R}^k$. However, due to numerical errors, the generated data may not lie exactly on the target level-set. Here, we propose to implement an additional post-processing step optionally in order to project the generated data onto the target level-set. Also refer to [33] for discussions on projection onto manifolds in the context of generative modeling. The first method is the projection to the closest point on the level-set, which amounts to solving

$$\bar{x} := \arg \min_{y \in \Sigma_z} \|x - y\|^2 \quad (22)$$

for each generated point x . However, unless the level-set Σ_z can be parametrized by certain coordinates, solving (22) is computationally infeasible because it is a constrained (high-dimensional) optimization task. Another simpler method is to project the generated state x along the ODE flow [49]

$$\frac{dY_t}{dt} = -\nabla G(Y_t), \quad Y_0 = x, \quad (23)$$

where the function $G : \mathbb{R}^d \rightarrow \mathbb{R}$ is defined as $G(y) := \frac{1}{2}\|\xi(y) - z\|^2$ for $y \in \mathbb{R}^d$. Thanks to the gradient structure, it can be shown that, under certain regularity assumptions on ξ , the quantity $G(Y_t)$ decreases to zero exponentially fast as $t \rightarrow +\infty$, implying that the state evolved by the flow of (23) approaches the level-set Σ_z . In practice, to perform the projection, it suffices to integrate the ODE (23) up to a time when certain criteria is met, i.e. $\|\xi(Y_t) - z\| < \epsilon_{\text{tol}}$, where $\epsilon_{\text{tol}} > 0$ is a small parameter specifying the tolerance.

4 Experiments

In this section, we demonstrate the capability of our approach through different representative datasets. The section is organized as follows: we first consider a synthetic dataset in \mathbb{R}^2 to illustrate the method. Next, we evaluate its performance on the trajectory data of the system under the Müller–Brown potential, a widely used benchmark system exhibiting metastability. Finally, we apply the approach to the alanine dipeptide molecular system, showcasing its applicability to molecular systems with complex energy landscapes. The neural network and the training were implemented using `PyTorch` [39].

4.1 2D Synthetic Dataset

The 2D dataset (Figure 1a) is sampled using the `make_circles` function from the package `scikit-learn` [40]. The CV map is defined as $\xi(x) = x_1^2 + x_2^2$ for $x = (x_1, x_2) \in \mathbb{R}^2$, whose empirical density is shown in Figure 1b.

The prior ν_{prior} is chosen as the standard Gaussian distribution in \mathbb{R}^2 . The vector field v in (10) is parameterized as a fully connected feedforward neural network, comprising a total of four layers: an input layer, two hidden layers with 128 neurons each and `Tanh` activations, followed by an output layer of size 2. The input consists of the spatial coordinate x in \mathbb{R}^2 , a time scalar t , and the target CV value z (with dimension 1). To learn the vector field v , the empirical objective $\mathcal{L}^{(N)}(v)$ in (13) is minimized using the Adam optimizer for up to 1000 epochs with early stopping (patience of 200), a learning rate of 10^{-3} , a weight decay of 10^{-4} , and a batch size of 1000. For other parameters, their default values in `PyTorch` were used.

Next, we evaluate the performance of the learned model for generating states conditioned on the value z . To this end, we choose the values of z uniformly within an extended range around the values visited in the dataset (with a 5% margin), and for each chosen value of z , 1000 new states are generated by integrating the ODE (10) using the `torchdiffeq` library [3] (4th-order Runge-Kutta scheme) up to $t = 1$ with 1000 time steps, starting from the standard Gaussian prior at $t = 0$. Based on the generated states, we estimate the mean value of ξ , the mean deviation of ξ from the target CV value z , defined as

$$\text{Deviation}(z) = \sqrt{\frac{1}{N} \sum_{i=1}^N (\xi(X^{(i)}) - z)^2}, \quad (24)$$

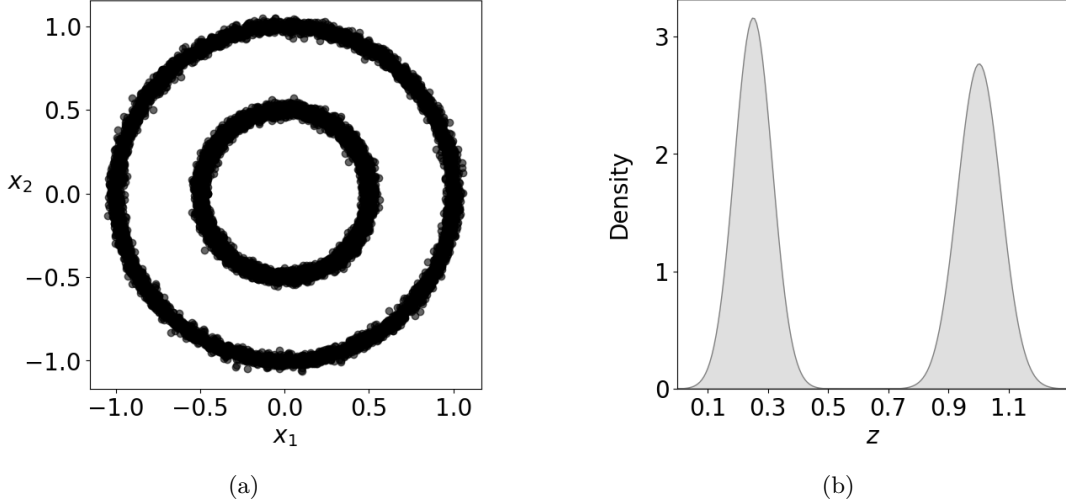


Figure 1: (a) Scatter plot of the original 2D dataset sampled using the `make_circles` function from `scikit-learn` [40]. (b) Density estimate of the corresponding CV map $\xi(x) = x_1^2 + x_2^2$.

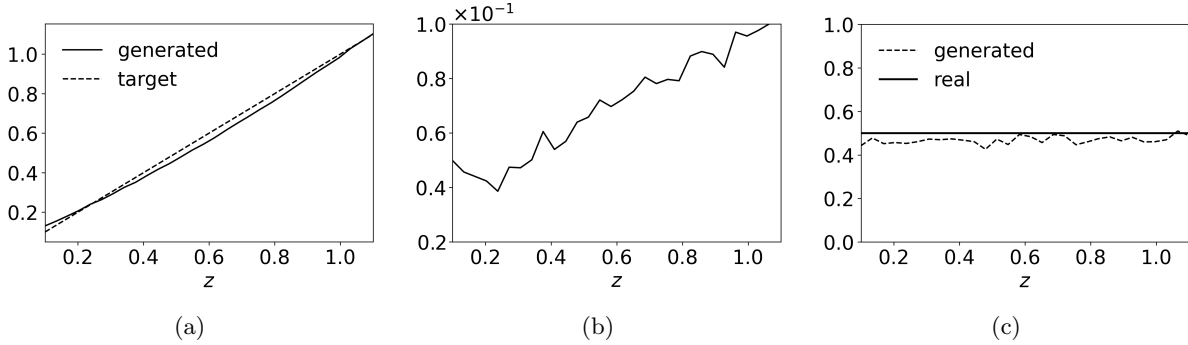


Figure 2: Results for the 2D dataset. (a) Mean value of ξ of generated samples compared to the intended CV value. (b) Mean deviation of ξ on generated samples from the target CV value. (c) Proportion of samples with positive x_1 values in the original and generated samples for different target CV values.

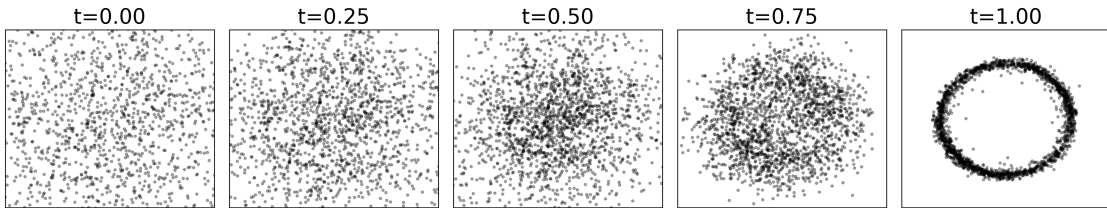


Figure 3: Evolution of the two-dimensional samples generated by the conditional ODE flow for a fixed target CV value $z = 0.6$. Each panel shows the particle positions at different integration times t , illustrating how the initial Gaussian cloud progressively morphs into the target distribution.

where $(X^{(i)})_{1 \leq i \leq N}$ are the generated samples, as well as the proportion of states with $x_1 \geq 0$, which are shown in Figures 2a, 2b, and 2c, respectively. The results in Figure 2 demonstrate that the proposed model performs consistently well across all evaluation metrics in the two-dimensional case. The generated CV values closely match the intended targets, the deviation remains low across the entire range of values, and the model accurately learns the conditional distribution.

Finally, Figure 3 presents the temporal evolution of the generated distribution for $z = 0.6$, obtained by integrating the ODE from a standard Gaussian initial cloud of 2000 points. Successive snapshots are taken at increasing integra-

tion times $t \in \{0, 0.25, 0.50, 0.75, 1.0\}$, showing how the initially isotropic Gaussian distribution gradually transforms into the target ring-shaped configuration.

4.2 Müller–Brown Dataset

We apply our approach to the two-dimensional Boltzmann–Gibbs distribution (1) with the Müller–Brown potential [38]. As shown in Figure 4, the potential has two deep wells (i.e. low-potential regions), separated by a shallow well. At low temperatures, the corresponding dynamics exhibits metastability with a curved transition pathway, making it an ideal model system for studying the complex behavior of metastable dynamics.

Model Description and Training. The dataset is prepared by sampling the trajectory of the overdamped Langevin dynamics (14) up to time $t = 600$ (corresponding to 3×10^6 steps), with the integration time step $\Delta t = 2 \times 10^{-4}$ and inverse temperature $\beta = 0.1$. The starting point is chosen in the deepest well, with configuration $(-0.6, 1.2)$. By recording states every 100 steps, we obtained a dataset consisting of 3×10^4 configurations.

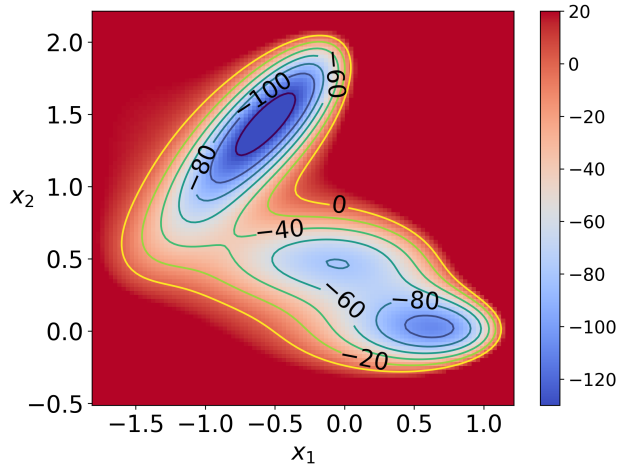


Figure 4: Heatmap and contour representation of the Müller–Brown potential landscape. The two major low-potential regions and the shallow low-potential region are shown in dark blue and light blue, respectively, while the contour lines highlight specific energy levels.

In order to define a CV map, we first trained an autoencoder with a one-dimensional bottleneck, modeled as a fully connected feedforward neural network, by minimizing the mean squared reconstruction error on the generated trajectory data. The encoder network consists of an input layer of size 2, three hidden layers of size 32 with **Tanh** activation, and an output layer of size 1. The decoder network consists of an input layer of size 1, a single hidden layer of size 32 with **Tanh** activation, and an output layer of size 2. Training was performed for 200 epochs using the Adam optimizer, with a learning rate of 10^{-3} and a batch size of 128. The CV map $\xi : \mathbb{R}^2 \rightarrow \mathbb{R}$ is defined by the trained encoder. Figure 5a shows the level-sets of ξ with the generated trajectory data superimposed, whereas Figure 5b shows the scatter plot of the potential energy $V(x)$ for each state x in the trajectory against the encoded CV value $\xi(x)$.

To test the enhanced learning technique discussed in Section 3.2, we also employed the ABF dynamics (20) with the learned CV map ξ , where the biasing force f_t was computed based on (21) on a uniform grid with grid spacing 0.1 that covers the range $[-2.6, 3.5]$. To ensure accurate estimation, the biasing force in a cell of the grid is applied to the system only after 100 samples have been used to estimate (21). The biased simulation was run for 1.5×10^5 steps and, after the initial 5×10^4 simulation steps (equilibration), states were recorded every 10 steps, resulting in a trajectory dataset of size 10^4 . Similarly to Figures 5a–5b, Figure 6a and 6b show the scatter plot of the biased trajectory data superimposed on the level-sets of ξ and the scatter plot of potential values $V(x)$ against the encoded CV value $\xi(x)$, respectively.

We trained our generative model (10) using the generated trajectory data and the learned CV map ξ . The vector field v is modeled by a fully connected feedforward neural network, which consists of an input layer of size 4 (i.e. the total dimension of the state $x \in \mathbb{R}^2$, time $t \in [0, 1]$ and the target CV value $z \in \mathbb{R}$), three hidden layers of size 128 with **Tanh** activation, and an output layer of size 2. Training was performed for 3000 epochs by minimizing the objective (13) (respectively, the empirical counterpart of (17) for biased trajectory data) using the Adam optimizer with a learning rate of 10^{-3} and a batch size of 512.

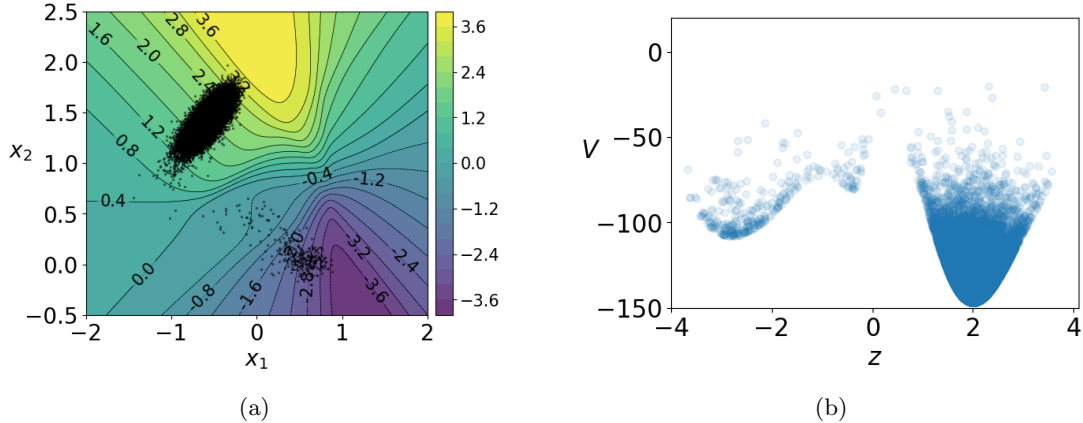


Figure 5: (a) Trajectory samples overlaid on level-sets of the learned CV map ξ . The color bar indicates the corresponding CV values across the configuration space. (b) Scatter plot of the potential energy versus the CV value.

Results. We evaluated the trained generative models by generating new states with prescribed target CV values $-2.0, 0.0$ and 2.0 . For each target CV value z , 10^3 states sampled from the two-dimensional standard Gaussian distribution were propagated by numerically integrating the ODE (10) using the `torchdiffeq` library [3] (4th-order Runge-Kutta scheme) up to $t = 1$ with 100 uniform time steps. The resulting final states at time $t = 1$ were interpreted as samples associated with the chosen CV value z . These samples are visualized in Figures 7a and 8a. Comparing these two figures reveals that the model trained using biased trajectory data produces spatially consistent samples distributed along the correct CV contours (Figure 8a), whereas the model trained using unbiased trajectory data tends to generate inconsistent samples when the target level-sets are not well covered by the training data (i.e. level-sets corresponding to $z = -2.0$ and $z = 0.0$ in Figure 7a). To quantify the evaluation, the encoded CVs of generated samples were compared to the target value z , and the root mean squared deviation defined in (24) was computed for a uniform grid of target values $z \in [-2.9, 3.6]$. The deviation curves in Figure 9 summarize this evaluation: the model trained on biased trajectories achieves a lower deviation across the CV range. Figure 10 shows snapshots of the temporal evolution of the point distributions under the learned flow model (10), taken at specific time points $t = 0.0, 0.5, 0.9, 0.95, 1.0$, illustrating the transformation from the initial standard Gaussian distribution to the final distribution conditioned on the latent variable z .

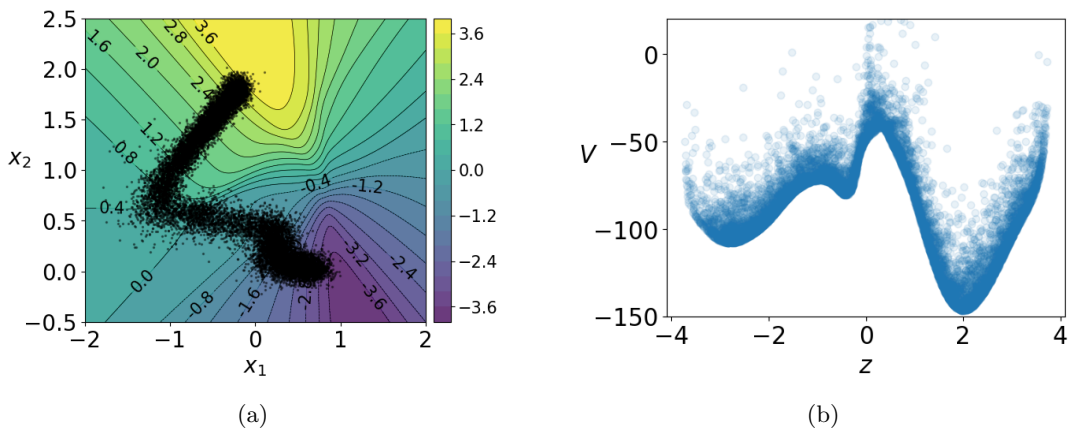


Figure 6: (a) Biased trajectory samples obtained from ABF simulation overlaid on level-sets of the learned CV map ξ . The color bar indicates the corresponding CV values across the configuration space. (b) Scatter plot of the potential energy versus the CV value for states in the biased trajectory.

We also tested the method introduced in Section 3.3 for projecting the generated samples. For each target CV value z , the samples obtained from the generative models (as shown in Figures 7a and 8a) were propagated by

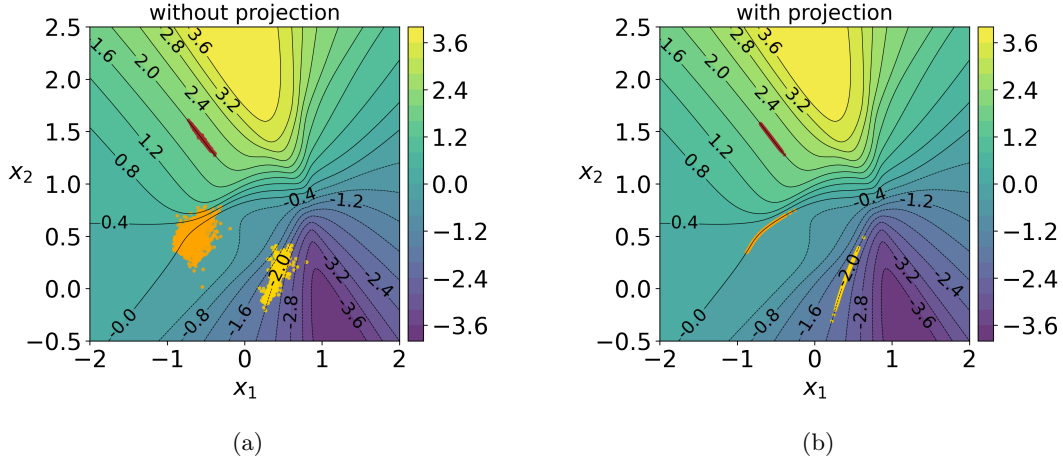


Figure 7: Generated samples for different CV values $z \in \{-2.0, 0.0, 2.0\}$ using the model trained on unbiased trajectory data. (a) Without projection. (b) With projection.

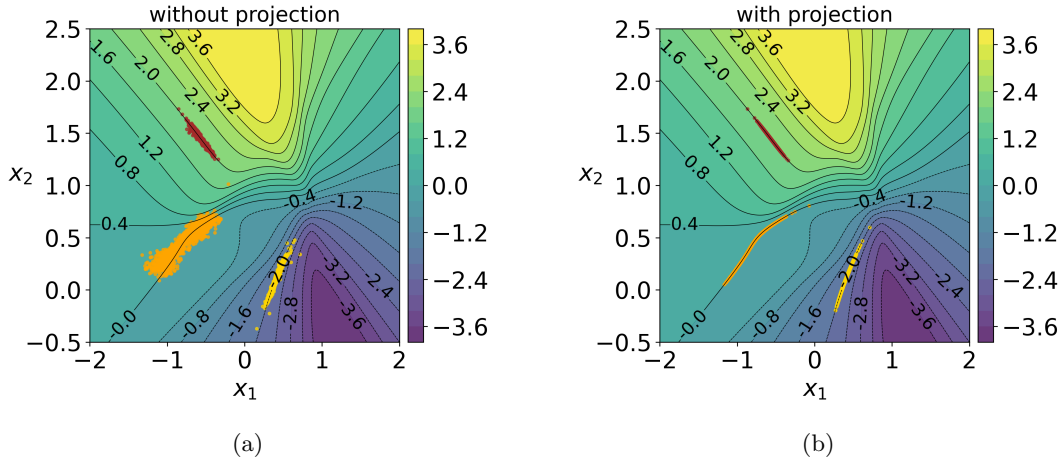


Figure 8: Generated samples for different CV values $z \in \{-2.0, 0.0, 2.0\}$ using the model trained on biased trajectory data. (a) Without projection. (b) With projection.

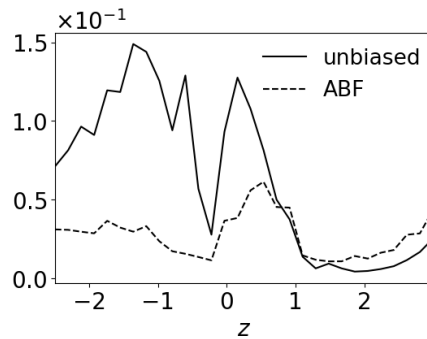


Figure 9: Comparison of the deviations defined in (24) for different target CV values between the model trained on unbiased trajectory data and the model trained on biased trajectory data (ABF).

numerically integrating the ODE 23 using the explicit Euler scheme, where we used step size 0.01, the maximal number of integration steps 7000 and tolerance $\epsilon_{\text{tol}} = 10^{-3}$. The resulting states are shown in Figures 7b and 8b, respectively,

from which we can conclude that the generated samples were successfully projected onto the corresponding level-sets.

Finally, we assessed the closeness between the empirical distribution of the generated samples and the conditional distribution on the corresponding level-set. We chose $z = -2.0$ and sampled 5×10^4 states on the corresponding level-set using the constrained sampling scheme in [5] with a step size 2.0×10^{-4} . Each state x was assigned the weight $|\nabla \xi(x)|^{-1}$, which is proportional to the likelihood ratio between the conditional distribution (3) and the invariant distribution of the constrained numerical scheme in the continuous-time limit, so that the weighted samples can be used to approximate the true conditional distribution on the level-set (see [5, 49] for detailed discussions). With these data, we estimated the densities of the first component x_1 for the samples generated by the learned generative model, their projections on the level-set by the method in Section 3.3, and the weighted samples obtained by constrained sampling. The results are shown in Figure 11a and Figure 11b for the model trained using unbiased trajectory data and the model trained using biased trajectory data, respectively. From these two figures, we can conclude that the projection step maps the generated states onto the level-set without modifying their distribution. Moreover, it can be observed that, compared to the model learned using unbiased trajectory data, the generative model learned using biased trajectory generates data whose distribution is closer to the true conditional distribution. We also computed probability densities of other quantities such as the potential energy and distance to the mean. The results are similar to those in Figure 11 and therefore are not shown here.

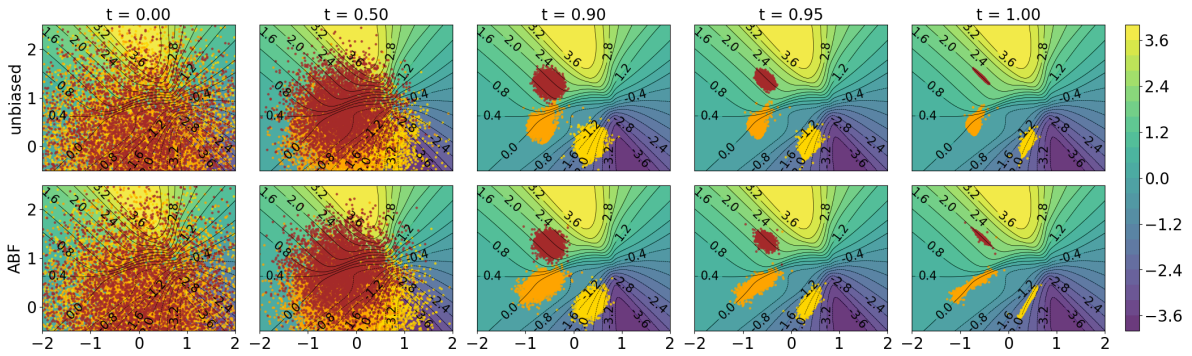


Figure 10: Time evolution of the data points under the learned model (10) for three different target values of $z \in \{-2.0, 0.0, 2.0\}$. The top part of the figure corresponds to the model trained with unbiased trajectory data, and the bottom part corresponds to the model trained with biased trajectory data. Contours and filled colormaps show the level-sets and the profile of the CV map ξ , respectively. Points corresponding to each z value are drawn in distinct colors to track their evolution over time.

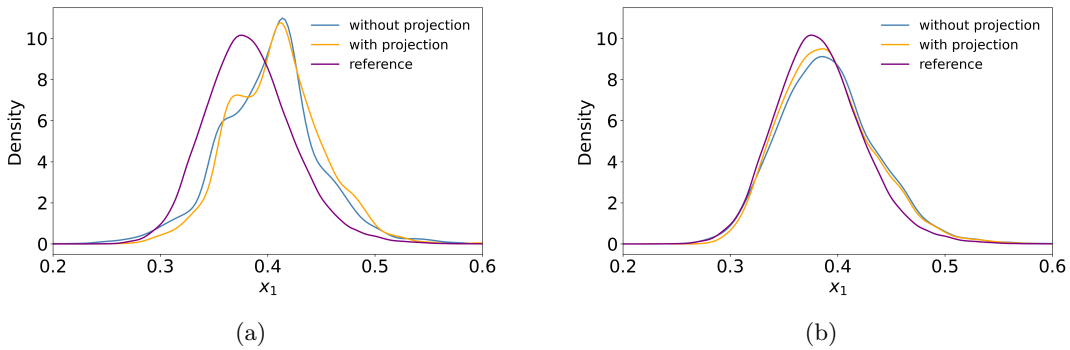


Figure 11: Density estimations of the first component x_1 for the samples generated using the generative model for the value $z = -2.0$ (without projection), their projections onto the level-sets (with projection), and the samples obtained by constrained sampling on the level-set (reference). (a) Results for the generative model trained using unbiased trajectory data. (b) Results for the generative model trained using biased trajectory data.

4.3 Alanine Dipeptide

Model Description and Training. In this study, we applied our generative approach to alanine dipeptide, which is a small benchmark molecular system consisting of 22 atoms. Our goal is to train the ODE model (10) for generative modeling of configurations of the system’s 10 non-Hydrogen atoms conditioned on its two backbone dihedral angles ϕ and ψ .

Trajectory data of the alanine dipeptide system were generated by performing molecular dynamics simulations for $t = 1500$ ns using the GROMACS package [47], where we adopted the same simulation parameters as in the previous work [24] and the states were stored every 10 ps, resulting in a trajectory dataset of 1.5×10^5 states. Only Cartesian coordinates of the 10 non-Hydrogen atoms were then extracted using MDAnalysis [12, 37] and aligned to a reference configuration via the Kabsch algorithm [20], thereby eliminating global translational and rotational motions. The aligned coordinates were then standardized by subtracting the empirical mean and dividing by the empirical standard deviation before being used as training data. Figure 12a shows the empirical density of the trajectory data projected onto the space of the two dihedral angles.

In addition to the unbiased MD data, we also generated an independent trajectory by performing an ABF simulation for $t = 500$ ns along the backbone dihedral angles ϕ and ψ . The ABF method applies a time-dependent biasing force to enhance the sampling of rarely visited regions of conformational space. The simulation was performed using the ColVars module [11] and the GROMACS package. The states were stored every 10 steps and the resulting trajectory dataset consists of 5×10^4 states. Figure 12b shows the empirical density of the trajectory data projected onto the space of the two dihedral angles. All ABF-biased coordinates were preprocessed in the same manner as the unbiased data—centered, aligned to a reference structure, flattened, and then standardized.

For the modeling of the vector field v in (10), we implemented a fully connected feedforward neural network that takes as input the atomic coordinates $x \in \mathbb{R}^{30}$, the temporal parameter $t \in [0, 1]$, and the CV value $z \in \mathbb{R}^2$, which correspond to the standardized values of (ϕ, ψ) . The feedforward network consists of five hidden layers with 512 hidden units and Tanh activations, while the output layer returns the vector field in \mathbb{R}^{30} .

The training of the vector field v was performed by minimizing the objective (13) for 1000 epochs, using the Adam optimizer with a learning rate of 10^{-3} , a batch size of 512, and default PyTorch parameters (e.g., for momentum coefficients, numerical stability parameter, and weight decay). After training, new samples in \mathbb{R}^{30} can be generated conditioned on the value of z (i.e. the target value of (ϕ, ψ)) by integrating the ODE (10) from random initial positions sampled from the standard Gaussian distribution. The generated samples are then denormalized and reshaped to obtain three-dimensional coordinates of the 10 non-Hydrogen atoms.

Results. To assess the quality of the generated conformations, we chose the target dihedral angles $(\phi, \psi) \in \{(-75^\circ, 150^\circ), (52.49^\circ, 34.95^\circ), (57.5^\circ, -126.78^\circ)\}$, which correspond respectively to the densely populated region, a secondary metastable region, and an isolated point in a low-population region in the dihedral angle space (see Figure 12a). For each of these values (ϕ, ψ) , we generated 1000 samples and identified the (reference) configuration in the trajectory whose dihedral angles are closest to (ϕ, ψ) . Root mean square deviation (RMSD) values of the generated samples from the reference were computed after Kabsch alignment. Histograms of RMSD values were constructed with fixed bin widths (0.02 \AA) to visualize the distribution of deviations in different regions represented by these values of dihedral angles. These distributions are shown for the model trained using the unbiased dataset in Figure 13 and for the model trained using the biased dataset in Figure 14, respectively.

RMSD distributions between nearby real structures are shown for the unbiased trajectory dataset in Figures 15a and 15b, serving as a baseline for intrinsic structural variability. In the left panel (Figure 15a), all pairs of configurations whose dihedral angles (ϕ_1, ψ_1) and (ϕ_2, ψ_2) satisfy $(\phi_1 - \phi_2)^2 + (\psi_1 - \psi_2)^2 < 1^\circ$ were identified using a nearest neighbors search in the dihedral angle space. For each pair, the RMSD was computed after Kabsch alignment to remove global translations and rotations. The right panel (Figure 15b) extends this analysis by binning the ϕ and ψ angles of configurations into a 50×50 grid and computing the mean RMSD of all conformations within each bin (empty bins were ignored). For the ABF-biased dataset, the same evaluation workflow was applied, and the results were nearly identical to those for the unbiased dataset. Comparing the histograms in Figure 13 and Figure 15, we can conclude that the mean deviations predicted by the trained model are of the same order as the intrinsic structural variability observed in the unbiased dataset.

To assess the angular consistency of the generated configurations across the dihedral space, we computed heatmaps of mean deviations (see (24)) per (ϕ, ψ) -bin for the generative models trained using both the unbiased and the ABF-biased datasets, as shown in Figure 16. For this analysis, the ϕ and ψ angles in the range $[-180^\circ, 180^\circ]$ were binned into intervals of equal length 20° , and the centers of each bin were used as target CV values. For each target CV value, $N = 200$ configurations were generated using the trained ODE models. The resulting mean deviations are shown in Figure 16a for the model trained using the unbiased trajectory data, where small deviations are concentrated in the high-probability regions of the CV space, and in Figure 16b for the model trained using the ABF-biased trajectory data, which exhibit uniformly low deviations across the full CV space.

Similarly to the previous example, the projection method introduced in Section 3.3 can be applied as a post-processing step to modify the generated configurations so that they satisfy the constraints on the target dihedral angles. We refer to the previous work [34, Appendices B.2 and B.4] for related numerical study.

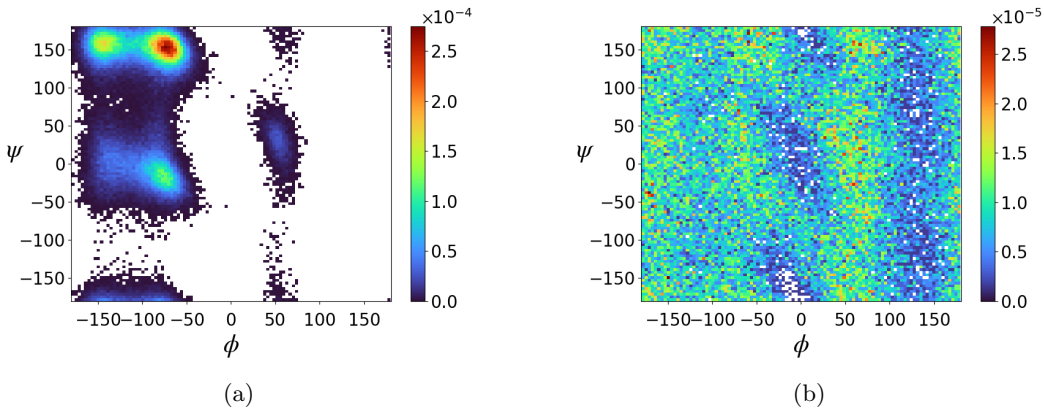


Figure 12: Empirical densities of the dihedral angles of the trajectory data. (a) Trajectory from unbiased simulation. (b) Trajectory from ABF simulation.

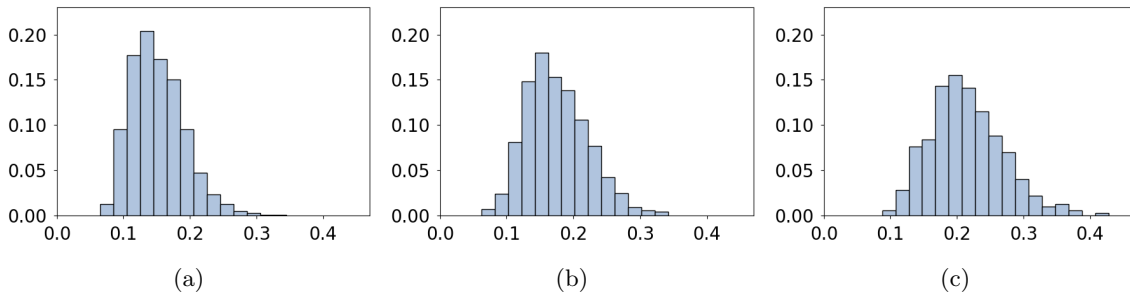


Figure 13: Results of the generative model trained with the unbiased dataset. Distributions of RMSD values (in Å) for generated samples at three representative CV locations: (a) $(\phi, \psi) = (-75^\circ, 150^\circ)$ in a well-populated region (b) $(\phi, \psi) = (52.49^\circ, 34.95^\circ)$ in the secondary metastable basin, and (c) $(\phi, \psi) = (57.5^\circ, -126.78^\circ)$ corresponding to an isolated point in the low-population region.

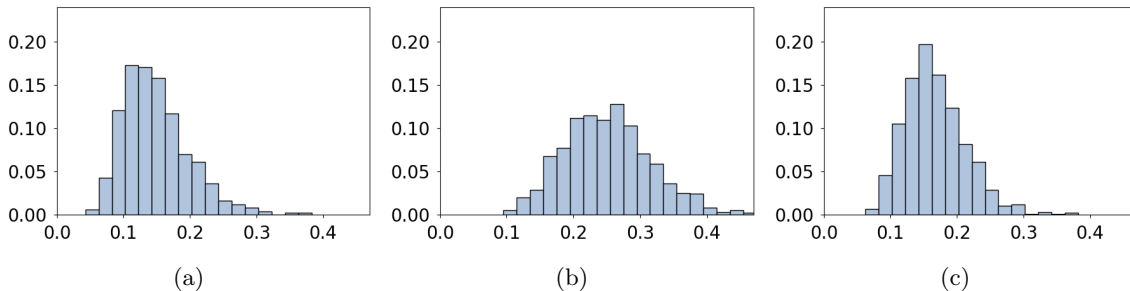


Figure 14: Results of the generative model trained with the ABF-biased dataset. Distributions of RMSD values (in Å) for generated samples at the same representative CV locations as in Figure 13: (a) $(\phi, \psi) = (-75^\circ, 150^\circ)$, (b) $(\phi, \psi) = (52.49^\circ, 34.95^\circ)$, and (c) $(\phi, \psi) = (57.5^\circ, -126.78^\circ)$.

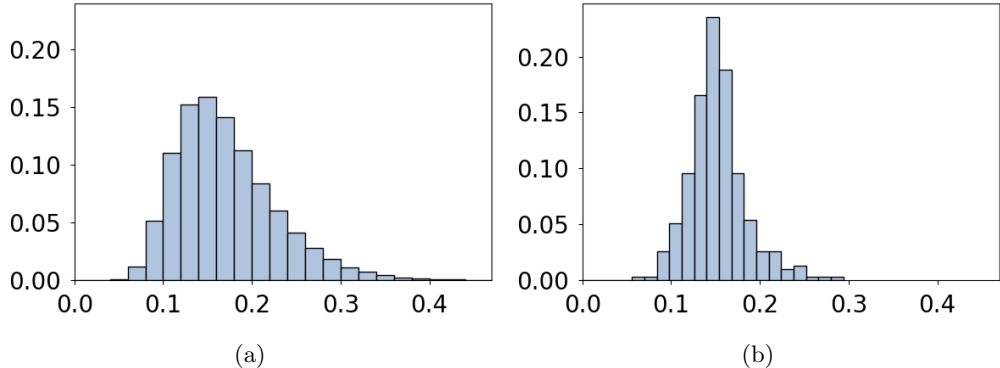


Figure 15: Analysis of intrinsic structural variability in the unbiased real dataset. (a) Distribution of RMSD values (in Å) between pairs of nearby configurations satisfying $(\phi_1 - \phi_2)^2 + (\psi_1 - \psi_2)^2 < 1$. (b) Histogram of mean RMSD values computed for each 50×50 (ϕ, ψ) -bin in the dihedral angle space, capturing spatial variations in local conformational variability.

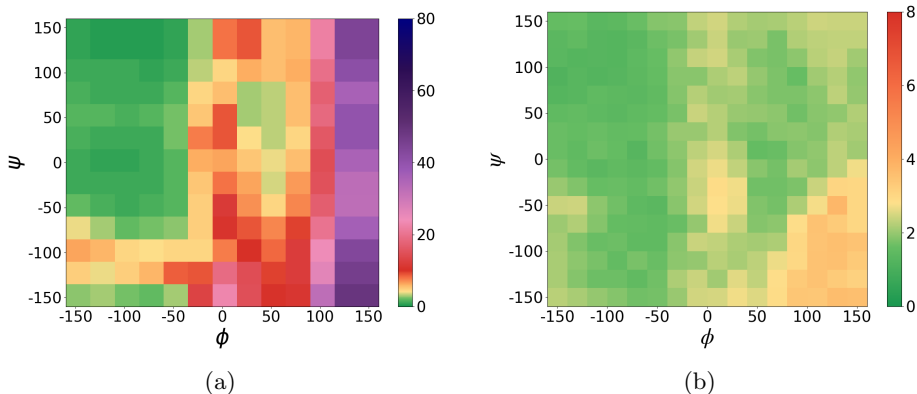


Figure 16: Heat maps of the mean deviation between the target CV value (ϕ, ψ) and the dihedral angles of generated configurations. (a) Unbiased molecular dynamics data. (b) ABF-biased data. Each pixel represents the mean circular distance in degrees, quantifying the accuracy with which the conditional generative model reproduces the desired angular constraints. Lower deviation indicates higher fidelity of the generated ensemble to the target CVs.

5 Conclusion

In this work, we have introduced a general framework for the generative modeling of conditional distributions on level-sets of CVs using flow-matching neural ODEs. By conditioning the learned flows on CV values, the model can generate samples across multiple level-sets without requiring explicit geometric information. To further enhance accuracy on level-sets in low-probability regions, we proposed to leverage biased trajectory data from enhanced sampling techniques such as ABF. Validation on concrete datasets demonstrates that our approach accurately reproduces conditional distributions and successfully exploits biased data to improve learning in sparsely sampled regions.

Beyond these results, this study opens several promising directions for future work. First, to better assess the effectiveness of the approach, it is meaningful to study the accuracy of the generative model by comparing certain distances between the generated distributions and the conditional distributions on level-sets. Second, a natural extension would be to combine the approach proposed in this work with methods that propagate the effective (reduced) dynamics in the CV space [21, 50]. Such a combination would lead to generative modeling approaches that can generate new trajectories of stochastic processes while taking into account the essential dynamics.

Overall, our study provides a general and practical approach for conditional generative modeling on manifolds defined by CVs, offering both methodological flexibility and the potential for applications in molecular modeling and beyond.

6 Acknowledgements

Fatima-Zahrae Akhyar acknowledges the Zuse institute Berlin for hosting her internship during which this research was conducted. Wei Zhang has been funded through DFG’s “Eigene Stelle” program (project 524086759) and has been supported by the DFG-grant CRC 1114 “Scaling Cascades in Complex Systems” Project Number 235221301. Gabriel Stoltz was funded by the European Research Council (ERC) under the European Union’s Horizon 2020 research and innovation programme (project EMC2, grant agreement No 810367), and was supported by Hi! PARIS and ANR/France 2030 program (ANR-23-IACL-0005). Christof Schütte has been supported through DFG-grant CRC 1114 (Project A04 “Efficient calculation of slow and stationary scales in molecular dynamics”, Project A05 “Probing scales in equilibrated systems by optimal nonequilibrium forcing”, Project B03 “Multilevel coarse graining of multiscale problems”, and Project C03 “Multiscale modelling and simulation for spatiotemporal master equation”).

References

- [1] M. S. Albergo and E. Vanden-Eijnden. Building normalizing flows with stochastic interpolants. In *International Conference on Learning Representations*, 2023.
- [2] H. Ben-Hamu, S. Cohen, J. Bose, B. Amos, M. Nickel, A. Grover, R. T. Q. Chen, and Y. Lipman. Matching normalizing flows and probability paths on manifolds. In *International Conference on Machine Learning*, volume 162, pages 1749–1763. PMLR, 2022.
- [3] R. T. Chen, Y. Rubanova, J. Bettencourt, and D. K. Duvenaud. Neural ordinary differential equations. *Advances in neural information processing systems*, 31, 2018.
- [4] R. T. Q. Chen and Y. Lipman. Flow matching on general geometries. In *International Conference on Learning Representations*, 2024.
- [5] G. Ciccotti, T. Lelièvre, and E. Vanden-Eijnden. Projection of diffusions on submanifolds: Application to mean force computation. *Commun. Pure Appl. Math.*, 61(3):371–408, 2008.
- [6] J. Comer, J. C. Gumbart, J. Hénin, T. Lelièvre, A. Pohorille, and C. Chipot. The adaptive biasing force method: everything you always wanted to know but were afraid to ask. *J. Phys. Chem. B*, 119(3):1129–1151, 2015.
- [7] E. Darve, D. Rodríguez-Gómez, and A. Pohorille. Adaptive biasing force method for scalar and vector free energy calculations. *J. Chem. Phys.*, 128(14):144120, 04 2008.
- [8] V. De Bortoli, E. Mathieu, M. Hutchinson, J. Thornton, Y. W. Teh, and A. Doucet. Riemannian score-based generative modelling. In *Advances in Neural Information Processing Systems*, volume 35, pages 2406–2422, 2022.
- [9] M. H. Duong, A. Lamacz, M. A. Peletier, A. Schlichting, and U. Sharma. Quantification of coarse-graining error in Langevin and overdamped Langevin dynamics. *Nonlinearity*, 31(10):4517, 2018.
- [10] L. C. Evans and R. F. Gariepy. *Measure Theory and Fine Properties of Functions, Revised Edition (1st ed.)*. Chapman and Hall/CRC, 2015.
- [11] G. Fiorin, M. L. Klein, and J. Hénin. Using collective variables to drive molecular dynamics simulations. *Mol. Phys.*, 111(22-23, SI):3345–3362, 2013.
- [12] R. J. Gowers, M. Linke, J. Barnoud, T. J. E. Reddy, M. N. Melo, S. L. Seyler, J. Domanski, D. L. Dotson, S. Buchoux, I. M. Kenney, et al. Mdanalysis: a Python package for the rapid analysis of molecular dynamics simulations. Technical report, Los Alamos National Laboratory (LANL), Los Alamos, NM (United States), 2019.
- [13] C. Hartmann. An ergodic sampling scheme for constrained Hamiltonian systems with applications to molecular dynamics. *J. Stat. Phys.*, 130(4):687–711, 2008.
- [14] J. Hénin, G. Fiorin, C. Chipot, and M. L. Klein. Exploring multidimensional free energy landscapes using time-dependent biases on collective variables. *J. Chem. Theory Comput.*, 6(1):35–47, 2010.
- [15] J. Hénin, T. Lelièvre, M. R. Shirts, O. Valsson, and L. Delemotte. Enhanced sampling methods for molecular dynamics simulations [article v1.0]. *LiveCoMS*, 4(1):1583, 2022.
- [16] M. Hirsch. *Differential Topology*. Graduate Texts in Mathematics. Springer New York, 2012.
- [17] J. Ho, A. Jain, and P. Abbeel. Denoising diffusion probabilistic models. In *Advances in Neural Information Processing Systems*, volume 33, pages 6840–6851, 2020.
- [18] C.-W. Huang, M. Aghajohari, J. Bose, P. Panangaden, and A. Courville. Riemannian diffusion models. In *Advances in Neural Information Processing Systems*, volume 35, pages 2750–2761, 2022.
- [19] J. Jo and S. J. Hwang. Generative modeling on manifolds through mixture of Riemannian diffusion processes. In *International Conference on Machine Learning*, volume 235, pages 22348–22370. PMLR, 2024.

- [20] W. Kabsch. A discussion of the solution for the best rotation to relate two sets of vectors. *Acta Cryst.*, 34(5):827–828, 1978.
- [21] F. Legoll and T. Lelièvre. Effective dynamics using conditional expectations. *Nonlinearity*, 23(9):2131–2163, 2010.
- [22] F. Legoll, T. Lelièvre, and S. Olla. Pathwise estimates for an effective dynamics. *Stoch. Process. Appl.*, 127(9):2841–2863, 2017.
- [23] F. Legoll, T. Lelièvre, and U. Sharma. Effective dynamics for non-reversible stochastic differential equations: a quantitative study. *Nonlinearity*, 32(12):4779, 2019.
- [24] T. Lelièvre, T. Pigeon, G. Stoltz, and W. Zhang. Analyzing multimodal probability measures with autoencoders. *J. Phys. Chem. B.*, (11):2607–2631, 2024.
- [25] T. Lelièvre, M. Rousset, and G. Stoltz. *Free energy computations: A mathematical perspective*. Imperial College Press, 2010.
- [26] T. Lelièvre, M. Rousset, and G. Stoltz. Langevin dynamics with constraints and computation of free energy differences. *Math. Comput.*, 81(280):2071–2125, 2012.
- [27] T. Lelièvre, M. Rousset, and G. Stoltz. Hybrid Monte Carlo methods for sampling probability measures on submanifolds. *Numer. Math.*, 143(2):379–421, 2019.
- [28] T. Lelièvre, G. Stoltz, and W. Zhang. Multiple projection MCMC algorithms on submanifolds. *IMA J. Numer. Anal.*, 43(2):737–788, 2023.
- [29] T. Lelièvre and W. Zhang. Pathwise estimates for effective dynamics: the case of nonlinear vectorial reaction coordinates. *Multiscale Model. Sim.*, 17(3):1019–1051, 2019.
- [30] A. Lesage, T. Lelièvre, G. Stoltz, and J. Hémin. Smoothed biasing forces yield unbiased free energies with the extended-system adaptive biasing force method. *J. Phys. Chem. B*, 121(15):3676–3685, 2017.
- [31] Y. Lipman, R. T. Q. Chen, H. Ben-Hamu, M. Nickel, and M. Le. Flow matching for generative modeling. In *International Conference on Learning Representations*, 2023.
- [32] X. Liu, C. Gong, and Q. Liu. Flow straight and fast: Learning to generate and transfer data with rectified flow. In *International Conference on Learning Representations*, 2023.
- [33] Z. Liu, W. Zhang, and T. Li. Improving the Euclidean diffusion generation of manifold data by mitigating score function singularity. *Advances in Neural Information Processing Systems*, 2025.
- [34] Z. Liu, W. Zhang, C. Schütte, and T. Li. Riemannian denoising diffusion probabilistic models. *under review*, 2025.
- [35] J.-M. Marin, P. Pudlo, C. P. Robert, and R. J. Ryder. Approximate Bayesian computational methods. *Stat. Comput.*, 22(6):1167–1180, 2012.
- [36] E. Mathieu and M. Nickel. Riemannian continuous normalizing flows. In *Advances in Neural Information Processing Systems*, volume 33, pages 2503–2515, 2020.
- [37] N. Michaud-Agrawal, E. J. Denning, T. B. Woolf, and O. Beckstein. Mdanalysis: a toolkit for the analysis of molecular dynamics simulations. *J. Comput. Chem.*, 32(10):2319–2327, 2011.
- [38] K. Müller and L. D. Brown. Location of saddle points and minimum energy paths by a constrained simplex optimization procedure. *Theor. Chim. Acta*, 53(1):75–93, 1979.
- [39] A. Paszke, S. Gross, F. Massa, A. Lerer, J. Bradbury, G. Chanan, T. Killeen, Z. Lin, N. Gimelshein, L. Antiga, et al. PyTorch: An imperative style, high-performance deep learning library. *Advances in Neural Information Processing Systems*, 32, 2019.
- [40] F. Pedregosa, G. Varoquaux, A. Gramfort, V. Michel, B. Thirion, O. Grisel, M. Blondel, P. Prettenhofer, R. Weiss, V. Dubourg, J. Vanderplas, A. Passos, D. Cournapeau, M. Brucher, M. Perrot, and E. Duchesnay. Scikit-learn: Machine learning in Python. *J. Mach. Learn. Res.*, 12:2825–2830, 2011.
- [41] N. Rozen, A. Grover, M. Nickel, and Y. Lipman. Moser flow: Divergence-based generative modeling on manifolds. *Advances in Neural Information Processing Systems*, 34:17669–17680, 2021.
- [42] U. Sharma and W. Zhang. Non-reversible sampling schemes on submanifolds. *Siam J. Numer. Anal.*, 59(6):2989–3031, 2021.
- [43] J. Sohl-Dickstein, E. Weiss, N. Maheswaranathan, and S. Ganguli. Deep unsupervised learning using nonequilibrium thermodynamics. In *International Conference on Machine Learning*, volume 37, pages 2256–2265. PMLR, 2015.

- [44] Y. Song and S. Ermon. Generative modeling by estimating gradients of the data distribution. In *Advances in Neural Information Processing Systems*, volume 32, pages 11895–11907, 2019.
- [45] Y. Song, J. Sohl-Dickstein, D. P. Kingma, A. Kumar, S. Ermon, and B. Poole. Score-based generative modeling through stochastic differential equations. In *International Conference on Learning Representations*, 2021.
- [46] S. Tavaré, D. J. Balding, R. C. Griffiths, and P. Donnelly. Inferring coalescence times from DNA sequence data. *Genetics*, 145(2):505–518, 1997.
- [47] D. Van Der Spoel, E. Lindahl, B. Hess, G. Groenhof, A. E. Mark, and H. J. Berendsen. GROMACS: Fast, flexible, and free. *J. Comput. Chem.*, 26(16):1701–1718, 2005.
- [48] E. Zappa, M. Holmes-Cerfon, and J. Goodman. Monte Carlo on manifolds: Sampling densities and integrating functions. *Commun. Pure Appl. Math.*, 71(12):2609–2647, 2018.
- [49] W. Zhang. Ergodic SDEs on submanifolds and related numerical sampling schemes. *ESAIM: Math. Model. Num.*, 54(2):391–430, 2020.
- [50] W. Zhang, C. Hartmann, and C. Schütte. Effective dynamics along given reaction coordinates, and reaction rate theory. *Faraday Discuss.*, 195:365–394, 2016.
- [51] W. Zhang and C. Schütte. Reliable approximation of long relaxation timescales in molecular dynamics. *Entropy*, 19(7), 2017.
- [52] W. Zhang and C. Schütte. On finding optimal collective variables for complex systems by minimizing the deviation between effective and full dynamics. *Multiscale Model. Simul.*, 23(2), 2025.